

# Impact of Warmer Eastern Tropical Pacific SST on the March 2015 Atacama Floods

DENIZ BOZKURT

*Center for Climate and Resilience Research, University of Chile, Santiago, Chile*

ROBERTO RONDANELLI AND RENÉ GARREAUD

*Department of Geophysics, and Center for Climate and Resilience Research, University of Chile, Santiago, Chile*

ANDRÉS ARRIAGADA

*Department of Geophysics, University of Chile, and Meteodata, Santiago, Chile*

(Manuscript received 25 January 2016, in final form 25 July 2016)

## ABSTRACT

Northern Chile hosts the driest place on Earth in the Atacama Desert. Nonetheless, an extreme precipitation event affected the region on 24–26 March 2015 with 1-day accumulated precipitation exceeding 40 mm in several locations and hourly mean rainfall rates higher than  $10 \text{ mm h}^{-1}$ , producing floods and resulting in casualties and significant damage. The event is analyzed using ERA-Interim, surface station data, sounding observations, and satellite-based radar. Two main conditions favorable for precipitation were present at the time of the event: (i) a cutoff low (COL) off the coast of northern Chile and (ii) positive sea surface temperature (SST) anomalies over the eastern tropical Pacific. The circulation driven by the COL was strong but not extraordinary. Regional Climate Model, version 4 (RegCM4), is used to test the sensitivity of precipitation to SST anomalies by removing the warm SST anomaly in the eastern tropical Pacific. The cooler simulation produced very similar COL dry dynamics to that simulated in a control run (with observed SST), but suppressed the precipitation by 60%–80% over northern Chile and 100% in parts of the Atacama Desert due to the decreased availability of precipitable water. The results indicate that the warm SST anomaly over the eastern Pacific, favored by the onset of El Niño 2015/16, was instrumental to the extreme precipitation event by providing an anomalous source of water vapor transported to Atacama by the circulation ahead of the COL.

## 1. Introduction

Northern Chile, a narrow strip of land between the subtropical southeastern (SE) Pacific and the Andes Cordillera ( $18^{\circ}$ – $26^{\circ}$ S, Fig. 1), features an extremely dry, stable climate hosting the Atacama Desert, widely regarded as the world's driest area outside of the polar

regions (e.g., Lettau and Lettau 1978; Middleton 2003; Rutllant et al. 2003; Garreaud et al. 2010; Rondanelli et al. 2015). Station-based, long-term mean annual precipitation is typically below 5 mm in coastal areas and low-level zones (up to 1000 m MSL) including values as low as  $0.05 \text{ mm yr}^{-1}$  at Quillagua, Chile ( $21.63^{\circ}$ S,  $69.52^{\circ}$ W), in the core of the hyperarid region (see Fig. 1a). High-altitude parts of Atacama ( $>3000 \text{ m MSL}$ ) receive more precipitation ( $10$ – $100 \text{ mm yr}^{-1}$ ) mostly during austral summer and associated with storms that are fed by moisture from the eastern side of the Andes (Houston 2006; Garreaud et al. 2010). The primary cause of Atacama aridity is the large-scale subsidence at subtropical latitudes, but it also has been related to local-scale features such as the steep coastal topography, the adjacent cold ocean, and locally descending circulations forced by the heating of the Andean slopes (e.g., Rutllant et al. 2003).

---

Denotes Open Access content.

---

Supplemental information related to this paper is available at the Journals Online website: <http://dx.doi.org/10.1175/MWR-D-16-0041.s1>.

---

*Corresponding author address:* Deniz Bozkurt, Center for Climate and Resilience Research, University of Chile, Blanco Encalada 2002, Santiago 8320000, Chile.  
E-mail: [dbozkurt@dgf.uchile.cl](mailto:dbozkurt@dgf.uchile.cl)

DOI: 10.1175/MWR-D-16-0041.1

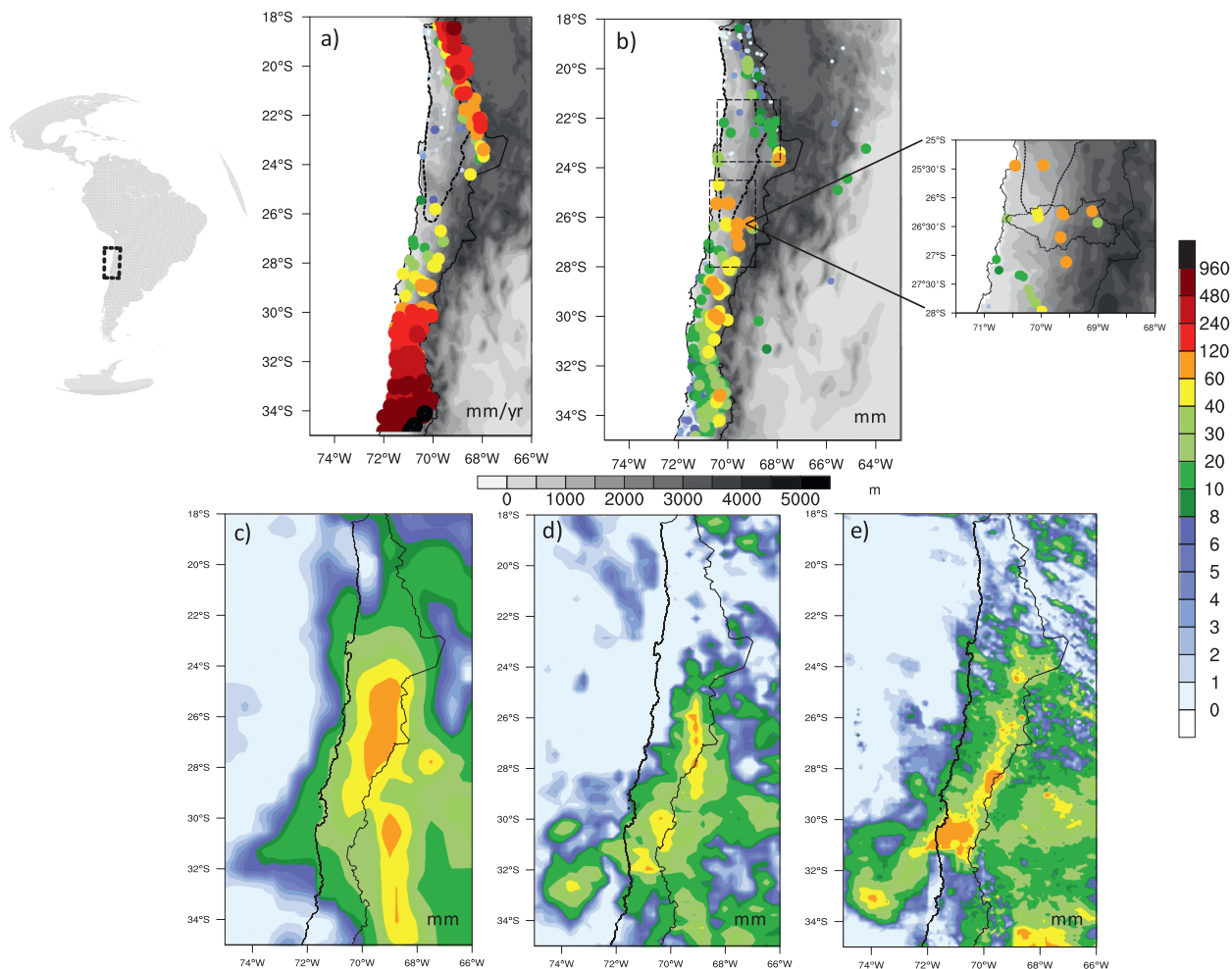


FIG. 1. (a) Mean annual observed precipitation ( $\text{mm yr}^{-1}$ ) and (b) 3-day (24–26 Mar 2015) accumulated precipitation (mm) from surface observations on a 5-min resolution topographic map derived from the NCAR “TerrainBase” (TBASE) dataset. Dashed borders in (a) and (b) identify the Atacama Desert [based on Olson et al. (2001)] and the Salado basin ( $\sim 26^{\circ}\text{S}$ ). Dashed boxes in (b) show two subregions of the local observations that are used for the model validation in section 3. Also included are 3-day (24–26 Mar 2015) accumulated precipitation (mm) for (c) ERAINT, (d) TRMM 3B42.V7, and (e) GPM (IMERG).

In spite of its extreme aridity, Atacama has witnessed significant precipitation events throughout history. For instance, during the 1877/78 strong El Niño year, several storms affected central and northern Chile and a storm produced floods around  $26^{\circ}\text{S}$  on 10 July 1877 (Vicuña-Mackenna 1877; Aceituno et al. 2009). Vargas et al. (2000) documented seven episodes of floods occurring in the city of Antofagasta, Chile ( $23.65^{\circ}\text{S}$ ,  $70.45^{\circ}\text{W}$ ), in the period between 1916 and 2000, mostly associated with the warm phase of ENSO. A recent event occurred on 17–18 June 1991—an ENSO neutral year—and resulted in 103 fatalities (Sepúlveda et al. 2006). On that night, within the span of a few hours, a total accumulated precipitation value of 42 mm resulted in flash floods and debris flows in most of the city (Garreaud and Rutllant 1996). Daily precipitation in excess of 30 mm also

occurred in the Copiapó Valley ( $27^{\circ}\text{S}$ ) in July 2011 (an ENSO neutral year) and June 1997 (a very strong El Niño year). Thus, while there is a tendency for more frequent rainfall events over northern Chile during El Niño years (Schulz et al. 2012), extreme events can occur in any phase of the ENSO cycle.

Most recently, between 18 and 27 March 2015, northern, central, and southern Chile experienced a series of extreme hydrometeorological events just at the beginning of the austral fall (Barrett et al. 2016; Wilcox et al. 2016). Within these dates an extreme precipitation event in Atacama occurred between 24 and 26 March 2015. During this 3-day period, accumulated precipitation exceeded 60 mm in several locations reaching up to 90 mm in the Río Salado basin ( $\sim 26^{\circ}\text{S}$ ; Fig. 1b). According to the latest report of the National Office of



Emergency of the Interior Ministry [Oficina Nacional de Emergencia del Ministerio del Interior (ONEMI)], the event left 31 dead, 16 people missing, 16 588 people affected, and major damage in the region's infrastructure (ONEMI 2015). In connection with barren and dry soil conditions, heavy rainfall over the steep mountainsides triggered flash floods and debris flows during the event. In contrast with flash floods in other arid regions (e.g., Rasmussen and Houze 2012; Kumar et al. 2014), there were no rainstorms before our case study that could have moistened the soil, indicative of a very rapid transfer from rainfall to runoff in the narrow valleys along the Atacama region.

The main synoptic-scale feature during the March 2015 event was a cutoff low (COL) pressure system that moved over northern Chile. COLs are upper-tropospheric closed lows that are completely detached from the westerlies and characterized by relatively cold air located in the mid- and upper troposphere (Palmén 1949; Hoskins et al. 1985). Cold air aloft may lead to convectively unstable conditions and severe surface weather has been associated with COLs over warm surface regions (e.g., Zhao and Sun 2007; Muller et al. 2008). Case and climatology studies reveal that the passage of COLs over northern Chile is not infrequent, there are about 4–6 cases per season, since the subtropical SE Pacific acts as a genesis region for these lows (Fuenzalida et al. 2005; Barahona et al. 2015). Furthermore, the presence of the Andes appears to delay the COL demise by blocking the inflow of warm, moist air from the interior of the continent (Garreaud and Fuenzalida 2007). Most of the COLs crossing northern Chile produce snowfall, very cold conditions, and strong winds in the high Andes (Vuille and Ammann 1997), but their effect (if any) is generally much less important at lower elevation. Yet, COL-generated precipitation accounts for 20%–40% of the mean annual precipitation in coastal and inland stations located in the region between 29° and 32°S and more than 40% in the coastal stations located in the southern edge of the Atacama Desert (Barahona et al. 2015).

As it turns out, the circulation driven by the COL that crossed northern Chile in late March 2015 was strong but not extraordinary, calling for additional ingredients to explain the extreme rainfall intensities and accumulations during this event. In particular, we focus our attention on the sudden increase in sea surface temperature (SST) along the tropical/subtropical west coast of South America that took place during the second half of March 2015 (Fig. 2), heralding the development of a strong El Niño event (Marshall et al. 2016). By 25 March, the SST in the Niño-1–2 region was 27.7°C, about 1.4°C over its mean climatological value at

precisely the time of the maximum of the seasonal cycle (Fig. 2a), triggering flooding in the rivers of northern Peru during the second half of March (ENFEN 2015) as often occurs during strong El Niño events (e.g., Takahashi 2004). A similar evolution of SST was observed off the coast of northern Chile (Fig. 2b) where our case study took place (+1.4°C anomaly on 25 March). We hypothesized that the anomalous SST warming along the coast of South America contributed to the magnitude and extent of the precipitation event over Atacama by providing an anomalous source of water vapor transported to northern Chile by the circulation ahead of the COL. Furthermore, we discuss how this SST anomaly played a role in the extremeness of the event by increasing either the convective instability or the baroclinicity of the system. To test our main hypothesis, we conducted a regional climate model experiment to explore the sensitivity of an extreme precipitation event to the warmer SST in the eastern tropical Pacific and shed light on the particular mechanisms.

The primary goals of the paper are to identify the characteristics and forcing mechanisms of the March 2015 Atacama floods and to disentangle the relative role of the eastern Pacific SST anomaly and the COL dry dynamics in explaining this extreme event at a regional scale. In spite of the rare occurrence of these events, a comprehensive investigation of the March 2015 Atacama floods through a combination of observational and reanalysis datasets as well as numerical simulations provides a guiding background to understand this event and its relationship to SST anomalies. Furthermore, the results of our study may be of relevance in view of increasing public awareness for other possible extreme events specifically during the ENSO episodes. Section 2 provides an overview of the event as well as the synoptic-scale description based on reanalysis, surface, and upper-air observations and satellite-based radar. We also performed a simple frequency analysis of dynamic and moisture features of the storm based on 35 years of reanalysis data. Section 3 describes the modeling setup and model validation, as well as the analysis of the results from two simulations that only differ from the surface boundary conditions. The conclusions are presented in the final section.

## 2. Event overview and synoptic description

### a. Data

The atmospheric circulation during March 2015 was analyzed using the European Centre for Medium-Range Weather Forecasts (ECMWF) interim reanalysis (ERA-Interim, hereafter ERAINT) data (Dee et al.

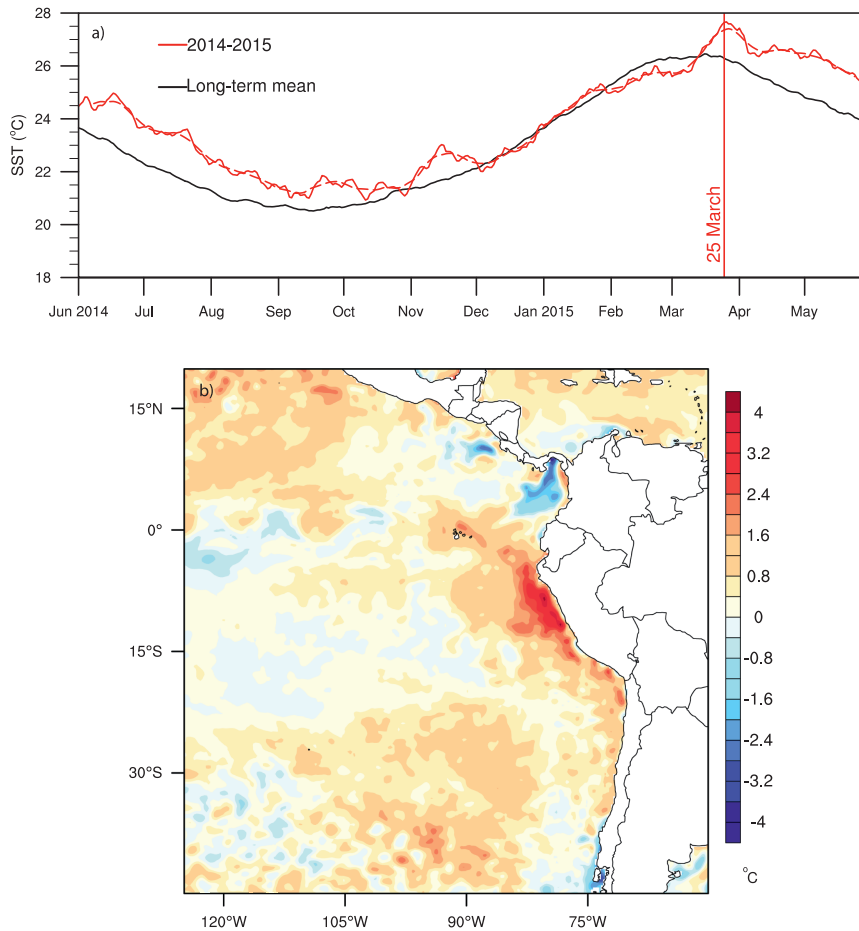


FIG. 2. (a) The NOAA OISST ( $0.25^{\circ} \times 0.25^{\circ}$ ; AVHRR based) daily SST values (red line) and long-term daily climatological mean (1982–2014; black line) for the Niño-1–2 region between June 2014 and June 2015. Red dashed line corresponds to 15-day running average. (b) Spatial map of 3-day (23–25 Mar 2015) average daily SST anomalies.

2011). Most reanalysis fields have a 6-h temporal resolution,  $0.75^{\circ} \times 0.75^{\circ}$  grid spacing, and 37 vertical levels. For precipitation, we use a bilinearly interpolated version of ERA-Interim on  $0.25^{\circ} \times 0.25^{\circ}$  latitude–longitude grid. Surface precipitation from rain gauges was obtained from the Chilean National Weather Service (Dirección Meteorológica de Chile), the Chilean Agency of Water (Dirección General de Aguas), the agrometeorological (AGROMET) weather network of the Ministry of Agriculture, and other private stations; see Fig. 1b for distribution of the stations. Furthermore, we use gridded data of Global Precipitation Measurement (GPM; IMERG) and Tropical Rainfall Measuring Mission (TRMM; 3B42.V7). Radiosonde soundings for Antofagasta between 15 and 31 March 2015 were obtained from the University of Wyoming repository (University of Wyoming 2015) and from the Chilean National Weather Service. To illustrate the convective nature of the precipitation we use

available infrared channel satellite images from *GOES-13* as well as available orbital data from the Global Precipitation Measurement mission Dual-Frequency Precipitation Radar (GPM-DPR; Hou et al. 2014) and from the TRMM Precipitation Radar (PR; Iguchi et al. 2000). Also data from the World Wide Lightning Location Network (WWLLN; Abarca et al. 2010) are used to identify lightning strikes over the course of the event.

#### b. Event overview

##### 1) RAINFALL DISTRIBUTION DURING THE EVENT

The extreme precipitation event in Atacama analyzed in this study took place between 24 and 26 March 2015, with 3-day accumulated values 10–100 times higher than the mean annual precipitation in this hyperarid region (Fig. 1b) producing flash floods and resulting in casualties and significant damage (ONEMI 2015). Significant precipitation affected a widespread area between  $23^{\circ}$

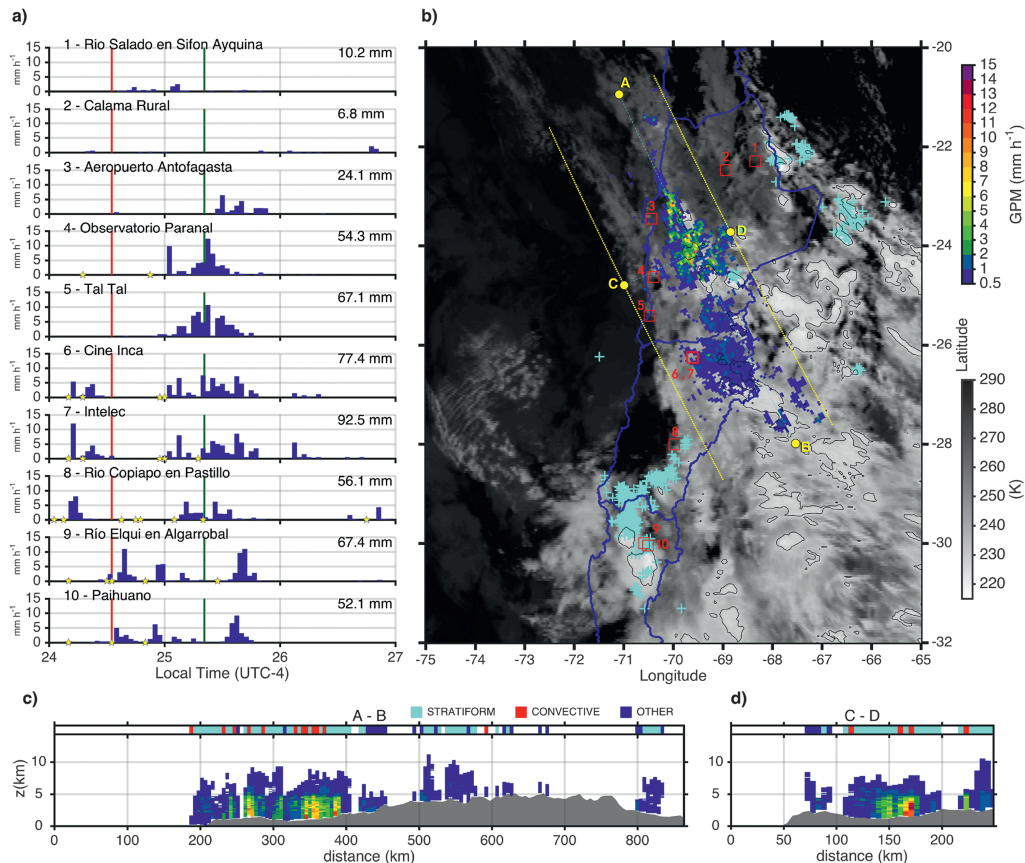


FIG. 3. (a) Hourly rainfall rates from selected stations and accumulated totals from 24 to 26 Mar 2015. Stars indicate lightning flashes during the corresponding hour in a radius of 5 km around each of the stations. Vertical red (green) line shows the GPM (TRMM) overpass time. (b) Snapshot of clouds, precipitation, and lightning at 1700 UTC 24 Mar from the passage of GPM. The location of the stations is indicated by numbered red squares. Brightness temperature is derived from *GOES-13* 11- $\mu\text{m}$  channel radiances at 1707 UTC and shown in grayscale (K). GPM-DPR near-surface rainfall rates at 1654 UTC are shown in color shading ( $\text{mm h}^{-1}$ ). Cyan plus signs indicate the location of lightning strikes from the WWLLN during 1650–1720 UTC. Parallel lines bound the limit of the GPM-DPR orbit swath. (c),(d) Classification of radar echoes along the vertical cross sections of rainfall along the transects shown in (b).

and 30°S from the coast to the Andes ridge. Total precipitation in the coastal region ranged between 10 and 60 mm and similar values were registered in the few stations located inland and over the western slope of the Andes. The highest accumulations—up to 90 mm in 2 days—took place in the Salado River basin ( $\sim 26^\circ\text{S}$ ) where the most damage and casualties due to flash floods occurred. Note that the highest accumulations occurred in the inland desert at elevations below 1500 m MSL, not at the top of the Andes ( $>4000$  m MSL in these latitudes) as often happens during summertime events (e.g., Garreaud et al. 2010).

Figure 3a shows the hourly distribution of rainfall for several selected stations. The stations to the south of 28°S (Cine Inca, Intelec, and Río Copiapó) recorded a first period of precipitation associated with lightning

during the morning hours on 24 March, with rainfall rates exceeding  $10 \text{ mm h}^{-1}$ , a break in the afternoon, and a second rainfall period during most of 25 March. Farther north, rainfall concentrated on 25 March, especially in Taltal and Paranal, Chile, where rainfall rates in excess of  $10 \text{ mm h}^{-1}$  were also observed for several hours suggesting anchored convective precipitation over the core of the Atacama Desert. Consistently, the major flooding events occurred on 25 March (ONEMI 2015).

The ERAINT precipitation field in Fig. 1c shows a reasonable agreement with the available surface stations, in terms of the area affected and location of the inland maximum. On the other hand, it overestimates the actual precipitation over Atacama and the Salado River basin (see Table S1 in the supplemental material). The TRMM 3B42 product does not show a good

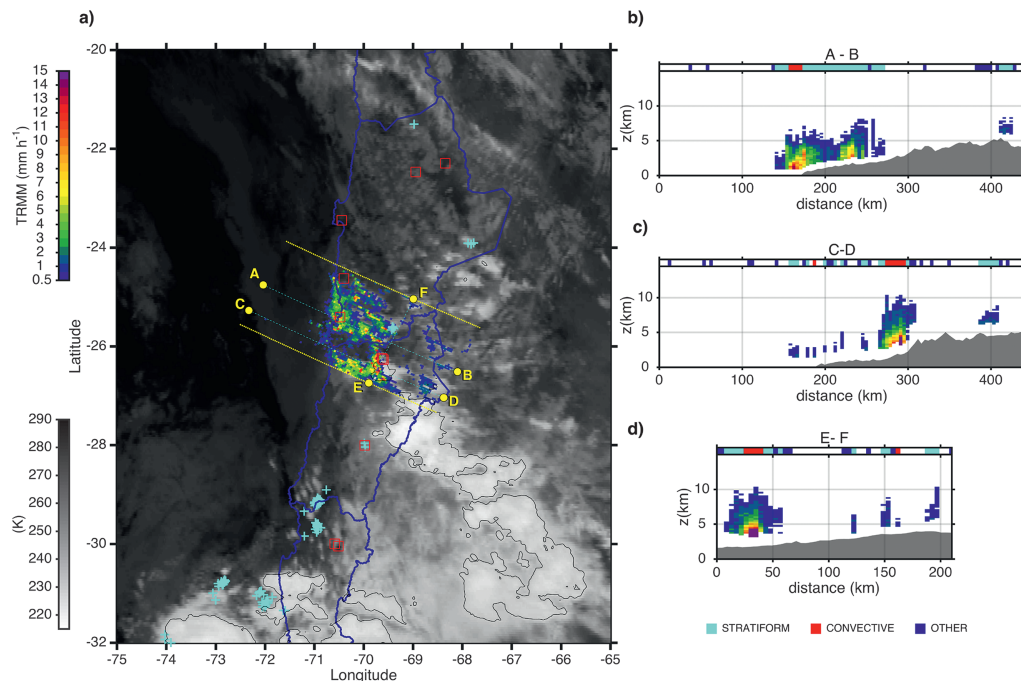


FIG. 4. (a) Snapshot of clouds, precipitation, and lightning at  $\sim 1100$  UTC 25 Mar from the passage of TRMM (vertical green line in Fig. 3a). Brightness temperature is derived from *GOES-13*  $11\text{-}\mu\text{m}$  channel radiances and shown in grayscale (K). TRMM PR near-surface rainfall rates are shown in color shading ( $\text{mm h}^{-1}$ ). Cyan plus signs indicate the location of lightning strikes from the WWLLN. Parallel lines bound the limit of the TRMM PR orbit swath. (b)–(d) Classification of radar echoes along the vertical cross sections of rainfall along the transects shown in (a).

agreement with the surface stations and misses much of the precipitation in the coastal areas to the north of  $26^{\circ}\text{S}$  and over Atacama (Fig. 1d). The reason behind the TRMM 3B42 underestimation is illuminated in the next section. The GPM (IMERG) gridded data show a better representation of precipitation distribution in the coastal areas and Atacama (Fig. 1e) than the TRMM 3B42 gridded product.

## 2) RADAR ORBITS

To illustrate the nature of the precipitation during this event we took advantage of two snapshots of the system taken by radar instruments on board the TRMM and GPM satellites. The passage of GPM over Atacama occurred at 1700 UTC 24 March, just at the end of the first period of rainfall noted in Fig. 3a. In Fig. 3b, rainfall is unequivocally present in the hyperarid region (almost entirely devoid of rain gauges) as a mesoscale convective band oriented northwest–southeast parallel to the upper-level flow driven by the COL. Surface rainfall rates are estimated from the GPM-DPR having maxima of  $\sim 10\text{ mm h}^{-1}$  embedded in a larger area of lower rainfall rates, concentrated at this time in the central plains of the Antofagasta region and associated with

relatively cold cloud tops ( $\sim 230\text{ K}$ ). Scattered lightning flashes are observed within the swath of the GPM orbit mostly near the higher Andes, although the most significant lightning activity at this time is located farther south between  $28^{\circ}$  and  $30^{\circ}\text{S}$ , outside the radar swath and associated with relatively warmer cloud tops. A classification of radar echoes is shown in the vertical cross sections in Figs. 3c and 3d. Convective echoes are concentrated along the slopes exposed to the northeasterly flow, with significant reflectivity up to 5 km.

A second radar orbit is available from the passage of TRMM at 1100 UTC 25 March (Fig. 4), concurrent with the second period of rainfall identified by the surface observations. This snapshot shows similar maximum rainfall rates on the order of  $10\text{ mm h}^{-1}$ , although isolated pixels show instantaneous rain rates of up to  $30\text{ mm h}^{-1}$  in the convective region, near point “E” in Fig. 4d. According to precipitation statistics from TRMM (e.g., Satoh et al. 2008) only 0.001% of the time rain rates are higher than  $30\text{ mm h}^{-1}$  in the tropical region within  $10^{\circ}\text{S}$ – $10^{\circ}\text{N}$ ,  $150^{\circ}\text{E}$ – $120^{\circ}\text{W}$ , which makes it truly remarkable in an arid region such as Atacama.

As on the previous day, deep convective echoes are concentrated along the coast (even a few tens of



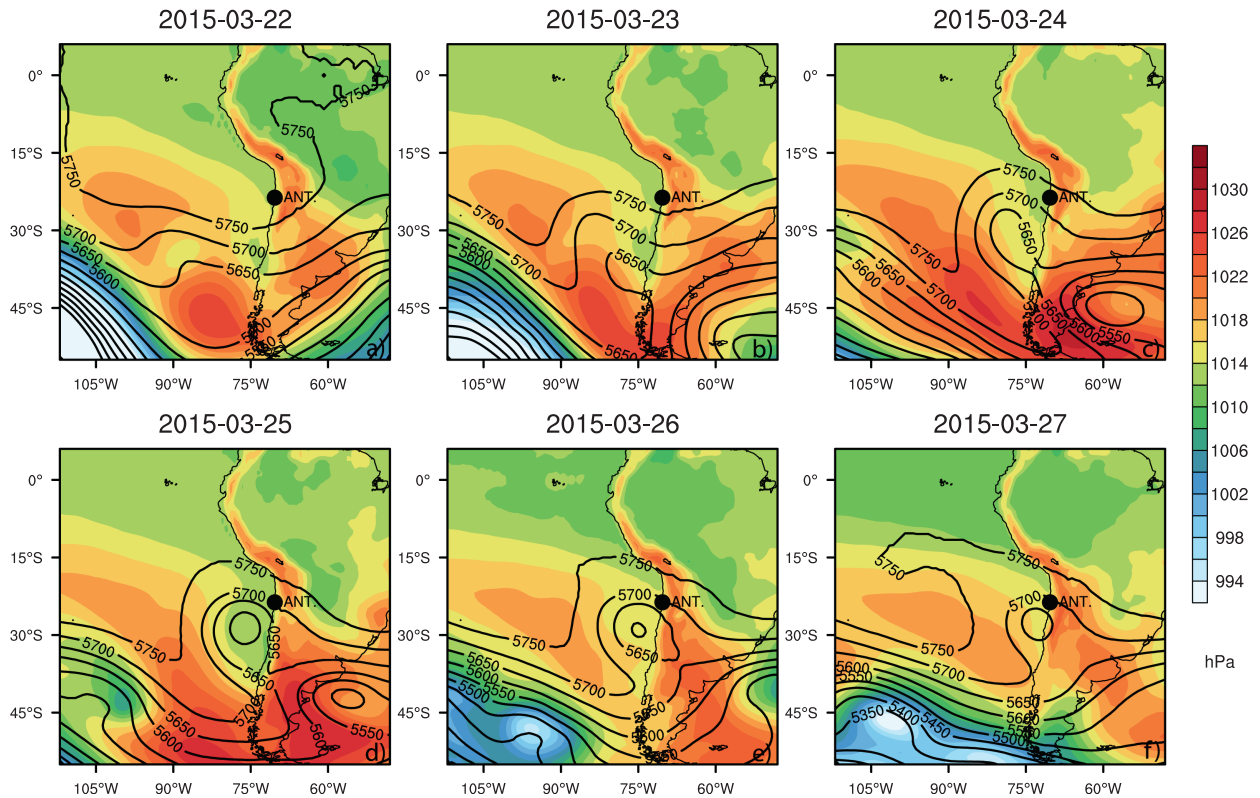


FIG. 5. Mean sea level pressure (hPa; shaded) and 500-hPa geopotential heights (m; contour lines) from ERAINT between 22 and 27 Mar 2015. The filled black circle shows the location of Antofagasta.

kilometers offshore) and the interior desert. In contrast, no rainfall was observed farther offshore or over the higher terrain of the Andes. This coastal maximum occurred associated with relatively warm cloud tops as shown in Fig. 4a with brightness temperatures significantly higher than 230 K. These warm cloud tops explain the low bias of rainfall estimations in satellite products that are based on infrared radiances such as TRMM 3B42. Both available space radar snapshots show little precipitation over the ocean, increasing sharply very close to the coast. This intriguing feature, which is also present in the high-resolution numerical simulations of the storm, points to an important role of coastal (or even Andean) topography in triggering the precipitation during this episode.

Sounding data at Antofagasta do reveal the presence of conditionally unstable layers in the lower troposphere but also convective inhibition ( $CAPE = 19.38 \text{ J kg}^{-1}$ ,  $CIN = -320 \text{ J kg}^{-1}$ ) on the afternoon of 24 March (see also next section). We infer then that the ascent over the coastal range (up to 1000 m MSL in some places) was instrumental in releasing intense, convective rainfall along the coast and farther inland, which subsequently transitioned to stratiform rainfall near the slope of the

Andes. During the course of the storm, the freezing level was located between 4000 and 4500 m MSL at  $\sim 26^\circ\text{S}$  (obtained from Antofagasta sounding and inferred from surface stations assuming a moist adiabatic lapse rate), resulting in a large catchment area for rainfall (as a comparison, the flooding event of June 1991 in Antofagasta occurred with a freezing level at about 2300 m MSL).

### 3) SYNOPTIC FIELDS FROM REANALYSIS

Figure 5 shows ERAINT daily mean sea level pressure and 500-hPa geopotential height between 22 and 27 March 2015. For most of this period, the midlatitude circulation over the SE Pacific was characterized by an intense, quasi-stationary surface anticyclone and a long-wave ridge aloft. At subtropical latitudes, a short-wave trough off the Chilean coast appeared on 22 March. In the next 24 h the trough deepened as it slowly moved eastward leading to a closed low by 24 March. The COL remained off the coast of northern Chile (with its center at about  $28^\circ\text{S}$ ) for the next 3 days reaching a minimum in geopotential by 25 March. In contrast with the well-defined closed low at mid- and upper levels only a weak surface trough was observed off the Chilean coast in the

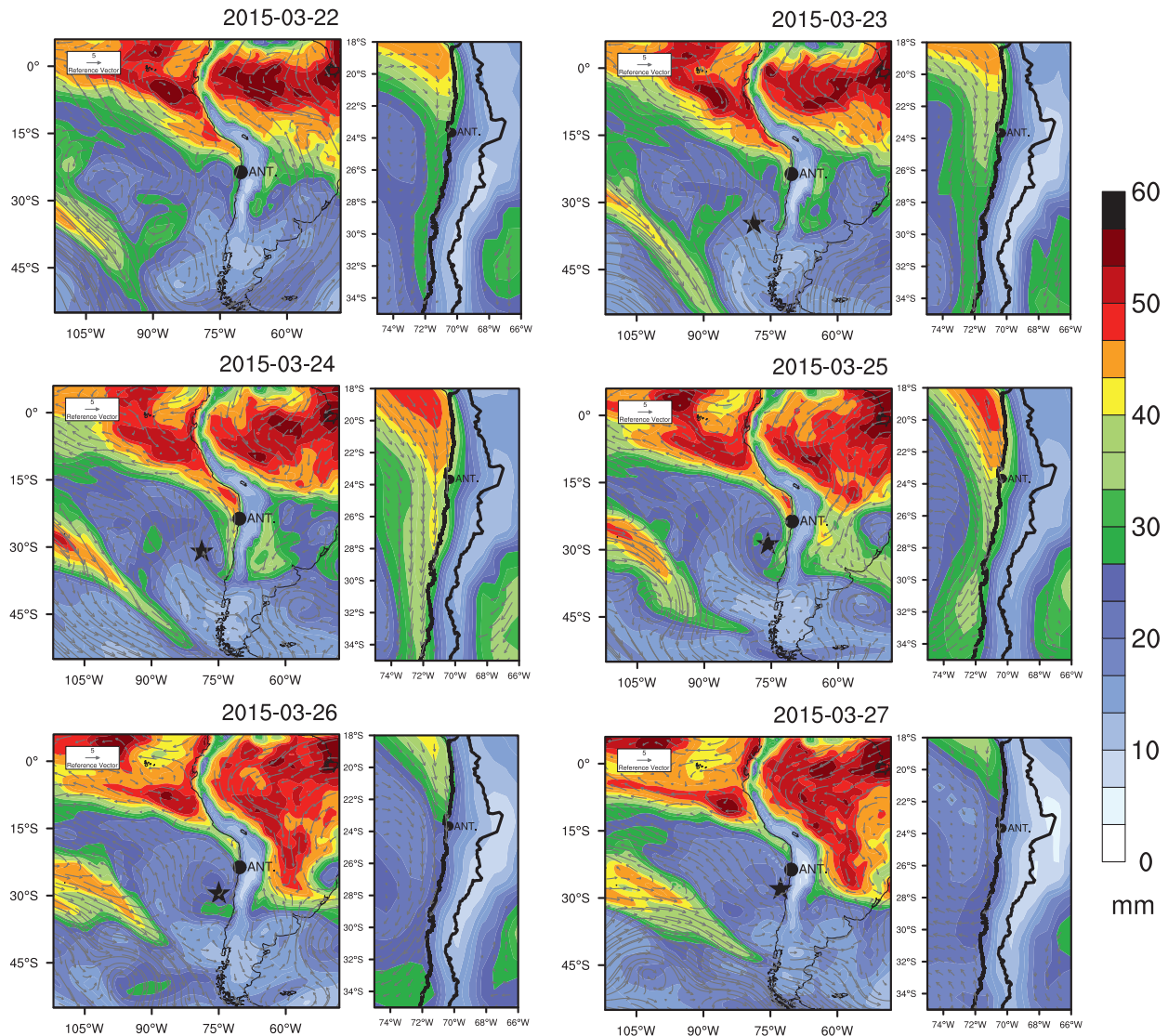


FIG. 6. PW (mm; shaded) and 850-hPa wind vectors from ERA-Interim for the whole domain and region of interest (northern Chile) between 22 and 27 Mar 2015. The 850-hPa wind vectors are masked with the topography. The filled black circle shows the location of Antofagasta and the filled black star shows the COL center at 500 hPa.

reanalysis data. This event followed the typical life cycle of COLs over the SE Pacific and had duration, scale, and displacement within their mean range (Fuenzalida et al. 2005). Nonetheless, there are two salient features in this case: (i) the COL grew up from a small short-wave trough, in contrast with more meridionally extended troughs in other cases (e.g., Garreaud and Fuenzalida 2007); and (ii) the anomalous intense midlevel ridge, surface anticyclone at higher latitudes over the South Pacific that persisted for several days, in connection with a wave train emanating from the western Pacific.

A low-level moistening in the coastal zone of northern Chile occurred in tandem with the development of northerly flow suggesting a key role of the horizontal

transport from lower latitudes. Such transport is well captured in Fig. 6 by daily maps of 850-hPa winds and vertically integrated water vapor [precipitable water (PW)]. The strong northwesterly low-level flow ahead of the COL center stretched a tongue of high PW air from the eastern tropical Pacific along the coast down to southern Peru and northern Chile. For instance,  $PW > 35$  mm was restricted to the north of 18°S on 22–23 March, but such values reached 30°S along a narrow coastal band by 25 March. A backward trajectory analysis (not shown) confirms that moist-laden air masses that arrived in northern Chile during 23–25 March resided over the Pacific ocean off northern Peru (5°–15°S) 1–2 days before. Recall that this region in the tropical

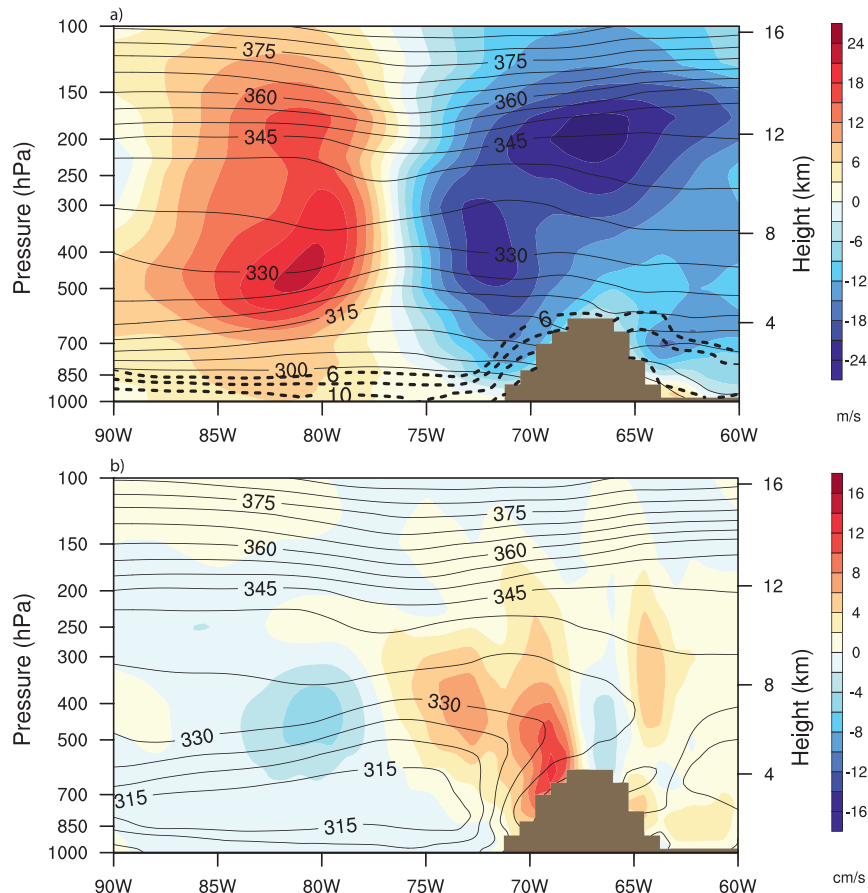


FIG. 7. (a) ERAINT longitude–pressure diagram at  $23.65^{\circ}\text{S}$  of  $\theta$  (K; solid contour lines),  $q$  ( $\text{g kg}^{-1}$ ; dashed contour lines), and  $v$  ( $\text{m s}^{-1}$ ; shaded) on 25 Mar 2015. (b) As in (a), but for  $\theta_e$  (K; contour lines) and vertical velocity ( $\text{cm s}^{-1}$ ; shaded) on 25 Mar 2015. The topographic profile was extracted from ERAINT.

Pacific experienced the largest SST warming during mid-March 2015 as shown in Fig. 2.

To illustrate the vertical structure of the COL, a longitude–pressure diagram at  $23.65^{\circ}\text{S}$  (the latitude of Antofagasta) of potential temperature  $\theta$ , meridional wind velocity  $v$ , and specific humidity  $q$  is shown in Fig. 7a. Near the time of maximum COL strengthening the cold core of the low was centered at about  $76^{\circ}\text{W}$ , spanning from 700 to 300 hPa. Above this layer the isentropes are downward indicative of a weak tropopause depression, whereas between the surface and 700 hPa there is little temperature perturbation. Nonetheless, the COL circulation completely eroded the strong low-level temperature inversion that characterized coastal northern Chile (e.g., Muñoz et al. 2011). Northerly and southerly horizontal winds are roughly symmetric with respect to the COL center, with maximum speeds in the middle troposphere ( $>20 \text{ m s}^{-1}$ ; around 400 hPa) in balance with the thermal field. A secondary northerly wind jet is found at about 200 hPa

just above the Andes crest. Note that the northerly–southerly couplet reaches down to the surface at the time of the stronger circulation in midlevels.

Quasigeostrophic, large-scale dynamics induce a fairly symmetric couplet of vertical motion around the COL center (e.g., Palmén 1949; Hoskins et al. 1985) with ascending motion ( $>10 \text{ cm s}^{-1}$ ) between 700 and 300 hPa offshore northern Chile (Fig. 7b). Over the western slope of the Andes there is another center of strong ascending motion ( $>16 \text{ cm s}^{-1}$ ) resulting from the mechanical uplift of the midlevel northwest flow impinging over the mountain range. Thus, both the synoptic-scale circulation and topographic effects resulted in a broad area of ascending motion over northern Chile from hundreds of kilometers offshore to the Andean crest.

Moist air (e.g.,  $q > 8 \text{ g kg}^{-1}$ ) is confined below 1 km MSL within the marine boundary layer over the SE Pacific but it expands up to about 3 km to the east of the COL center (Fig. 7a). A cursory examination of ERAINT specific humidity at times other than this

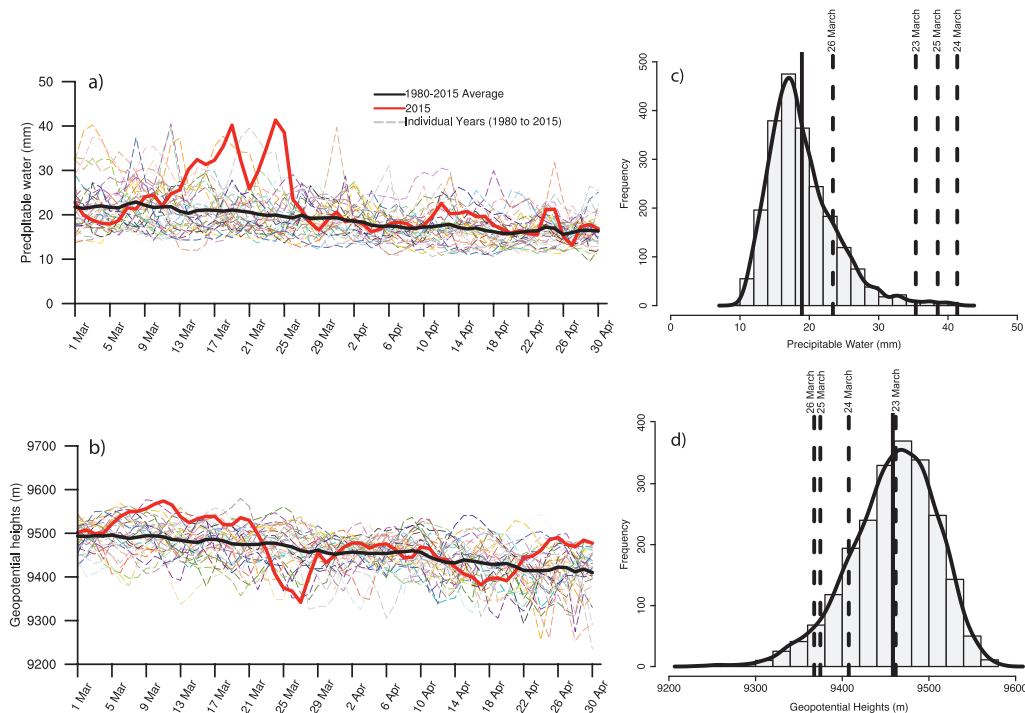


FIG. 8. (a) March–April daily time series of ERAINT PW (mm) and (b)  $z_{300}$  (m) over Antofagasta. The solid lines indicate the 1980–2015 (black) and 2015 (red) mean fields. (c) The frequency distribution of ERAINT daily precipitable water and (d)  $z_{300}$  for March–April between 1980 and 2015. The vertical solid line corresponds to the mean and the vertical dashed lines correspond to event days between 23 and 26 Mar.

storm reveals that the presence of moist air atop of the Andes of northern Chile is exceptional, showing further evidence of inland water vapor transport by the northwesterly circulation in the leading edge of the COL. The moistening of the lower troposphere and the marked upward cooling below the COL center leads to conditionally unstable conditions off the coast of Atacama. Indeed, the vertical cross section of equivalent potential temperature  $\theta_e$  (Fig. 7b) and Antofagasta sounding data reveals layers of  $d\theta_e/dz \leq 0$  in the lower troposphere on 24 and 25 March. Thus, ascent of moist-laden, conditionally unstable air masses over the coastal range and farther inland were able to trigger convection, producing the episodes of high rainfall rates that punctuated the long-lived, stratiform precipitation periods.

### c. Time series and frequency analysis

In closing this section we explore how unusual the thermodynamic and dynamic conditions were during the March 2015 extreme precipitation event in Atacama. To this effect we use two key variables over the historical record available from ERAINT: PW for thermodynamic condition and 300-hPa geopotential heights  $z_{300}$  for dynamic aspects of the COL. ERAINT data compared against sounding observations at Antofagasta for

three months (January–March) of 2015 show good agreement and capture the time evolution of the March 2015 event for specific moisture (500 and 850 hPa), precipitable water, and meridional wind speed (300 hPa) (see Fig. S4 in the supplemental material). Furthermore, evaluation of ERAINT against sounding observations over other mountain areas (e.g., Tibetan Plateau) indicates a good quality and reliability with small root-mean-square errors and small mean biases (Bao and Zhang 2013).

Figure 8a shows the March–April daily time series of PW and  $z_{300}$  from ERAINT for each year between 1980 and 2014 as well as their long-term mean. The time evolution of PW during 2015 indicates high PW values beginning during the second week of March reaching a maximum on 24 March 2015 (41.33 mm, with a departure of 21.4 mm from the mean field). The time evolution of  $z_{300}$  (Fig. 8b) shows a sudden decrease on 21 March and low values continued for the next few days reaching a minimum by 25 March, with a departure of  $>100$  m from the mean field. The values of PW and  $z_{300}$  during the March 2015 event stand out very clearly from the background values observed in the last 35 years.

Figures 8c and 8d show the frequency distribution of ERAINT daily PW and  $z_{300}$ , respectively, considering



all days for March and April between 1980 and 2015. The reanalysis PW distribution is positively skewed, with a mean of  $\sim 20$  mm and 80% of the daily values in the 12–30-mm range. The highest PW value (41.33 mm) did occur on 24 March 2015. The PW was also very high on 25 March (38 mm). The 3-day (24–26 March) averaged PW anomaly (see Fig. S3 in the supplemental material), reveals that the high moisture was present all along the coastal area of southern Peru and northern Chile, as hinted by the actual PW values in Fig. 6. The  $z_{300}$  shows a left-tailed distribution with a mean of  $\sim 9460$  m. According to this analysis, the upper-level dynamic conditions during the March 2015 event were anomalous but not extreme (e.g., 9407 m on 24 March). Analyses of other metrics of the COL circulation (e.g., upper-level winds and core temperature anomalies) led to similar conclusions.

Thus, in the context of the 35 years of reanalysis data the event of March 2015 features the most extreme moist conditions (as per PW) during austral fall in coastal northern Chile. By the contrary, strong but not extreme dynamical conditions (e.g.,  $z_{300}$ ) during the event indicate a rather ordinary circulation around the COL. Noted that PW was also high on 19 March, but  $z_{300}$  values were near normal, emphasizing that both high moisture availability and strong dynamical forcing are needed to create an extreme rainfall event in northern Chile.

### 3. Numerical simulations

#### *a. Model description and experiment design*

In this section we attempt to isolate the role of eastern tropical Pacific warming around the second week of March 2015 on the COL evolution and precipitation over Atacama. In principle, such SST anomaly could provide additional water vapor to feed the storm by increasing humidity within the maritime boundary layer. Alternatively, SST might destabilize the troposphere allowing deep convection to occur. However, the actual SST anomaly off northern Chile was relatively minor compared with that on northern Peru coasts. To test the impact of the SST anomalies on the COL evolution and resulting precipitation, we conducted a numerical experiment using Regional Climate Model, version 4 (RegCM4), a three-dimensional, primitive equation, hydrostatic regional climate model developed by the International Centre for Theoretical Physics.

Granted, RegCM4 does not resolve explicitly the convective clouds that were actually present in the Atacama storm and produced the highest rainfall rates. Here we relied on well-established convective parameterizations (e.g., the Grell and Emanuel schemes; see

details next) and verified the ability of the model in simulating the observed precipitation field. Indeed, RegCM has been used in numerous regional climate model simulations, many of them over regions dominated by convective precipitation (e.g., Wang et al. 2003; Smiatek et al. 2009; Davis et al. 2009; Sylla et al. 2011; Giorgi et al. 2012) and it was integrated with a horizontal grid spacing of 10 km enough to resolve down to the impressive regional relief.

We also emphasize that the main objective of this modeling effort is to examine our hypothesis on the role of the warm tropical SST rather than a detailed examination of the mesoscale storm dynamics that would have required a cloud-resolving simulation. In any case, we also compared our RegCM4 results against a non-hydrostatic simulation with a 2-km horizontal resolution using the Weather Research and Forecasting (WRF) Model performed by Departamento de Geofísica, Universidad de Chile (2015) (see Fig. S1 and Table S1 in the supplemental material).

RegCM4 is the latest version of the modeling system originally developed by Giorgi et al. (1993a,b) and Pal et al. (2007). It is a limited-area model and its dynamical core is based on the hydrostatic version of the Fifth-generation Pennsylvania State University–National Center for Atmospheric Research Mesoscale Model (MM5; Grell et al. 1994). Multiple physical schemes are available in the model. In the present study RegCM4 runs are performed using 1) the land surface model Biosphere–Atmosphere Transfer Scheme (BATS) of Dickinson et al. (1993); 2) the planetary boundary layer of Holtslag et al. (1990); 3) the radiative scheme of the NCAR Community Climate System Model, version 3 (CCSM3; Kiehl et al. 1996); 4) the ocean flux parameterization of Zeng et al. (1998); and 5) the scheme of Pal et al. (2000) for representing resolvable precipitation. In terms of cumulus parameterization, there are several options for convective precipitation in RegCM4: the Kuo-type scheme of Anthes (1977), the Grell scheme (Grell 1993), the Emanuel scheme (Emanuel 1991), and mixed schemes. Based on a couple of test simulations done with different convective schemes, we employ the mixed scheme (Grell scheme over ocean and Emanuel scheme over land) for the present study, as it produced a spatial precipitation distribution that more closely resembles the observed field. A more detailed description of the model and physical parameterizations can be found in Giorgi et al. (2012).

For the modeling experiment, a one-way nesting approach was applied on two domains at 60- (mother,  $192 \times 224$  grid cells) and 10-km (nested,  $560 \times 520$  grid cells) grid spacing using a rotated Mercator projection (Fig. 9). Initial and lateral boundary conditions for the

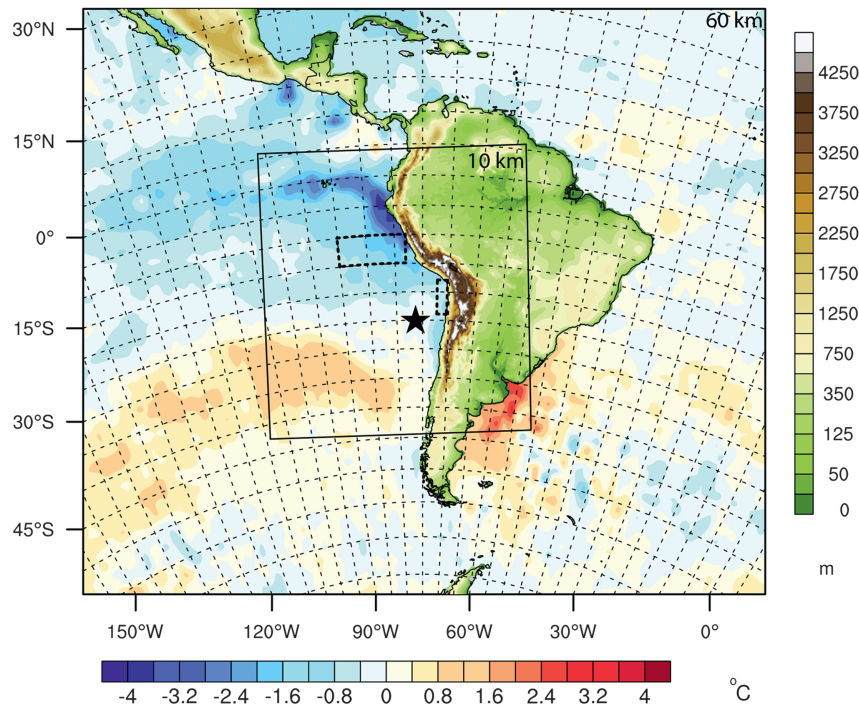


FIG. 9. Topography (m) in the nested configuration with two domains at 60- and 10-km resolutions together with differences ( $^{\circ}\text{C}$ ) between SST input fields of sensitivity simulation and control simulation for 25 Mar 2015. The filled black star shows the COL center at 500 hPa based on ERAINT.

mother domain were provided by ERAINT available at 6-h intervals with a grid spacing of  $1.5^{\circ} \times 1.5^{\circ}$  (Dee et al. 2011). The nested domain was then forced by the 3D atmospheric outputs of the mother domain. A total of 12 grid points in each direction were allocated for each lateral buffer zone in which the model prognostic variable were nudged to the boundary conditions with an exponential nudging coefficient proposed by Giorgi et al. (1993b). ERAINT SST fields (6 hourly,  $1.5^{\circ} \times 1.5^{\circ}$ ) were used as surface boundary conditions.<sup>1</sup>

The simulations were performed during 1–31 March 2015 for the mother domain and 15–31 March 2015 for the nested domain. The modeling experiment includes a control simulation (CTR) that uses the observed SST fields and a sensitivity simulation (SENS) that maintains the observed SST field of 10 March 2015 (just before the sudden coastal warming; Fig. 2) for the rest of the simulation period. By doing so, SENS has a surface

boundary condition (SST) cooler than its CTR counterpart over the eastern tropical Pacific (about  $4^{\circ}\text{C}$  along the Peruvian coast by the time of the COL development; Fig. 9). SENS is also slightly cooler (from  $0^{\circ}$  to  $-0.4^{\circ}\text{C}$ ) than CTR below the COL center and slightly warmer (less than  $+0.8^{\circ}\text{C}$ ) farther south. Thus, the results from SENS depict the evolution of the COL—and the attending precipitation—that would have occurred in absence of the mid-March warming off the coast of South America.

#### b. Model validation

We first examine the synoptic conditions in CTR by showing 500-hPa geopotential heights and wind vectors during the precipitation event (Fig. 10a). The development of the COL to the north of the midlatitude ridge in CTR is in agreement with that described in section 2. Nonetheless, the simulated COL center is about  $4^{\circ}$  to the north of the observed (ERAINT) center and the simulated 500-hPa geopotential height at the maximum of the COL intensity has a central value of 5300 m, which is about 300 m below ERAINT. This negative bias is unlikely to significantly affect the dynamics of the simulated COL in the CTR, given that it is approximately homogenous around the perturbation. Furthermore,

<sup>1</sup> Several test simulations were carried out by using different initial and boundary conditions and SST dataset such as NCEP–NCAR reanalyses and OISSTv2; however, the best performing configuration was achieved by ERAINT in terms of COL circulation and location and PW distribution.

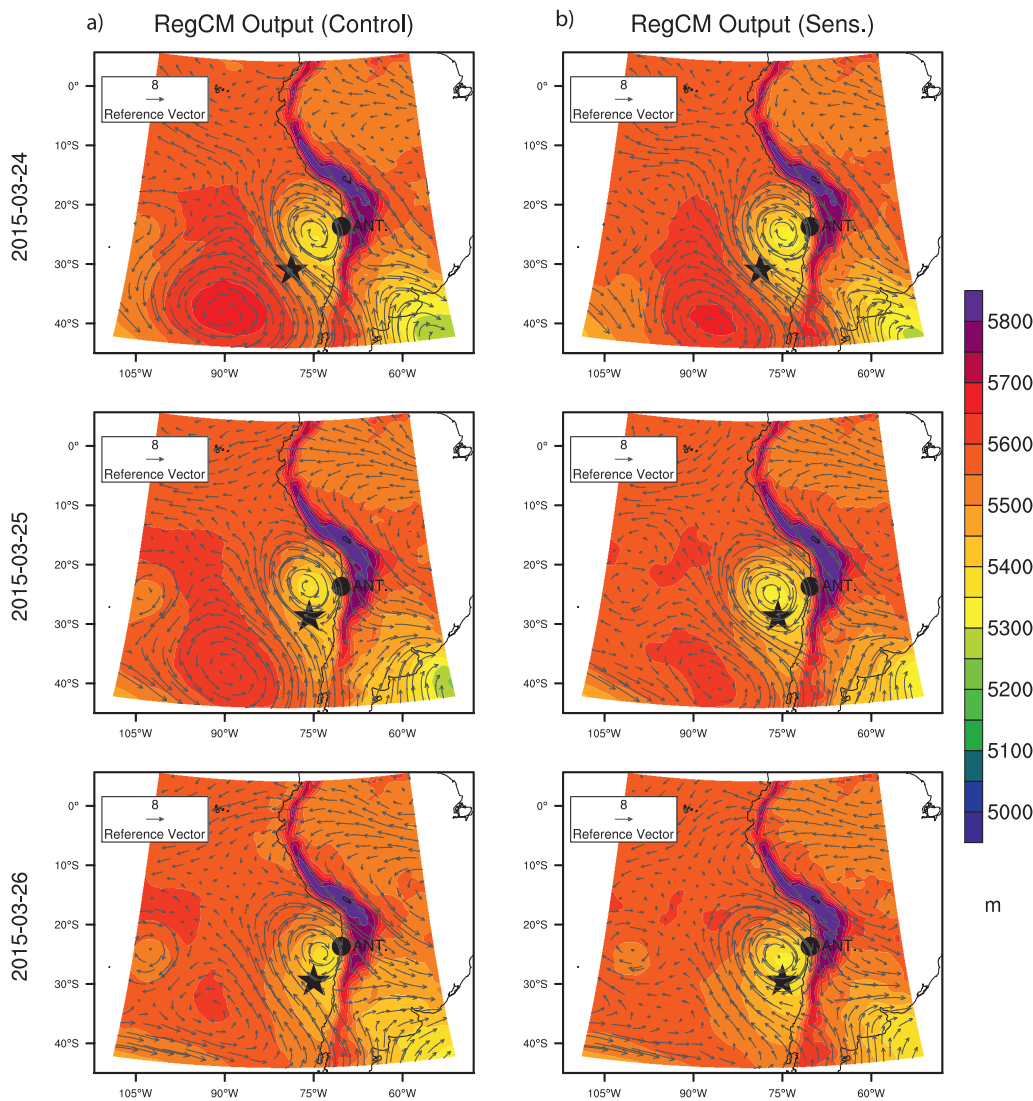


FIG. 10. (a) CTR and (b) SENS of 500-hPa geopotential heights (m; shaded) and wind vectors ( $\text{m s}^{-1}$ ) for 24–26 Mar 2015. The filled black circle shows the location of Antofagasta and the filled black star shows the COL center at 500 hPa based on ERAINT.

since our main focus is to study the sensitivity to changes in surface SST, a reasonable representation of the circulation and precipitation in the CTR run will suffice for our purpose. The similarity between CTR results and ERAINT is found in other upper-level meteorological fields and is consistent with the continuous nudging that provides the lateral boundary conditions.

Figure 11a shows the CTR values of PW (contours) for 25 March. The model reproduces well the spatial pattern of the PW found in ERAINT (Fig. 6), including the tongue of moist air extending from the tropical Pacific to the central Chile coast in connection with the northerly low-level flow to the east of the COL center. CTR, however, underestimates PW, relative to

ERAINT, across much of the domain. Off the northern Chile coast, CTR has a precipitable water of  $\sim 35$  mm compared with more than 40 mm in ERAINT and Antofagasta sounding.

Finally, let us consider the precipitation field simulated by RegCM4. Figure 12a shows the 3-day (24–26 March) accumulated precipitation in CTR. Overall, the CTR precipitation agrees quite well with the observed pattern (Fig. 1b) over Atacama and the simulated values match the observations over the arid zone well. More specifically, we compare the model precipitation with the local observations for two subregions in northern Chile. Figure 12b presents the scatter diagram of 3-day accumulated precipitation from the

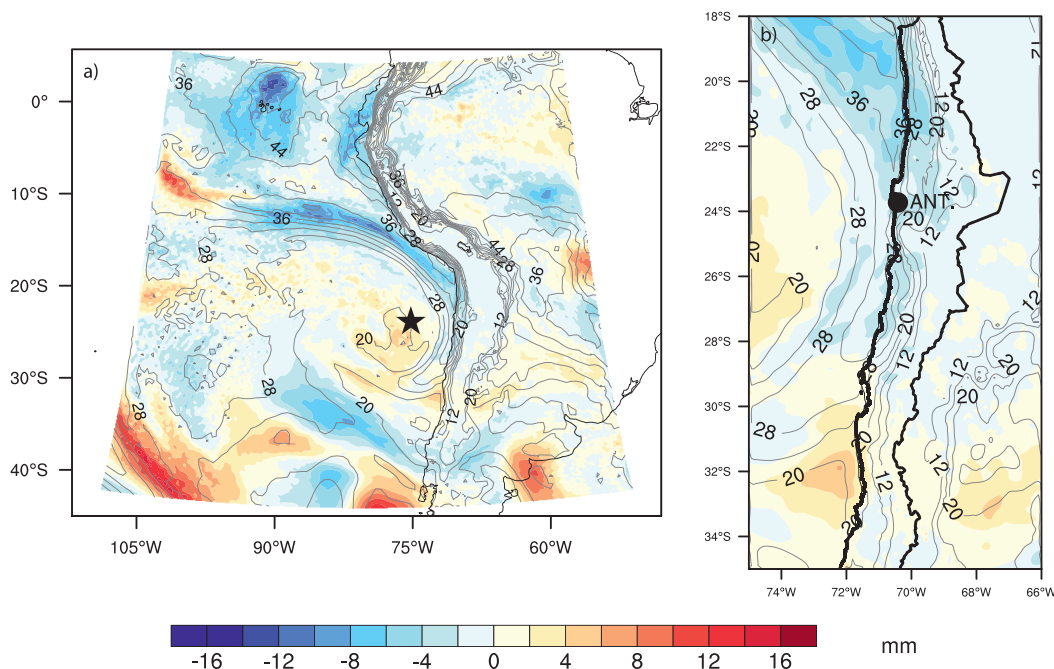


FIG. 11. (a) The 25 Mar 2015 PW differences (mm; shaded) between SENS and CTR for the whole domain. The contour lines correspond to the PW of CTR (mm). The filled black star shows the COL center based on CTR at 500 hPa. (b) As in (a), but for the region of interest (northern Chile).

observations versus simulated precipitation in the corresponding grids, revealing a close fit to the 1:1 line in both subregions ( $28^{\circ}$ – $24.5^{\circ}$ S and  $24^{\circ}$ – $21.5^{\circ}$ S). Nonetheless, the 3-day accumulated precipitation is underestimated by RegCM4 in the southern parts of northern Chile ( $-7.67$  mm) with higher root-mean-square error (RMSE) ( $18.29$  mm), and slightly overestimated in Atacama ( $+2.07$  mm) with lower RMSE ( $8.69$  mm).

The observed west–east variation of the 3-day accumulated precipitation at  $26^{\circ}$ S (based on available stations at this latitude) shows that precipitation is maximized over the interior desert near the western slope of the Andes (Fig. 12c). The simulated precipitation along this zonal transect reasonably reproduces the orographic enhancement of the precipitation albeit with a systematic underestimation. The reason why RegCM4 underestimates precipitation to the southern parts of northern Chile is perhaps related to the lower PW amount transported from the north along the coast and inconsistencies in the COL center during the event in the simulation. Furthermore, the lack of a nonhydrostatic model framework would be another factor contributing to the underestimation of orographic enhancement in RegCM4 over the southern parts of northern Chile.

As noted before, cores of intense convective rainfall embedded in stratiform precipitation and orographic enhancement were an important ingredient of the

Atacama storm. A high-resolution ( $2$  km), non-hydrostatic simulation of this event using WRF was performed by Departamento de Geofísica, Universidad de Chile (2015). The 3-day accumulated precipitation simulated by WRF captures the large accumulations over the slope of the Andes in northern Chile, similar to that in the RegCM4 simulations (see Fig. S1 in the supplemental material). RegCM4 CTR has biases quite similar to WRF (see Table S1 in the supplemental material) and both models show a band of coastal precipitation south of Antofagasta, that extends offshore a few tens of kilometers. This is a mesoscale feature that is present in the radar orbital data shown in Fig. 4a and in both the RegCM4 and WRF simulations. The good representation of even these mesoscale features lends further support to the use of RegCM4 for our modeling experiment described in the next section.

### c. Sensitivity experiment

Figure 10a shows the simulated 500-hPa geopotential height at selected times during the storm in both CTR (discussed before) and SENS (Fig. 10b). Notably, the COL's circulation, position, and intensity in SENS are very similar to their CTR counterparts. The agreement between SENS and CTR is evident in the sequence of 500-hPa wind maps but also within the whole troposphere. For instance, profiles of zonal and meridional wind in both CTR and SENS in two different regions of



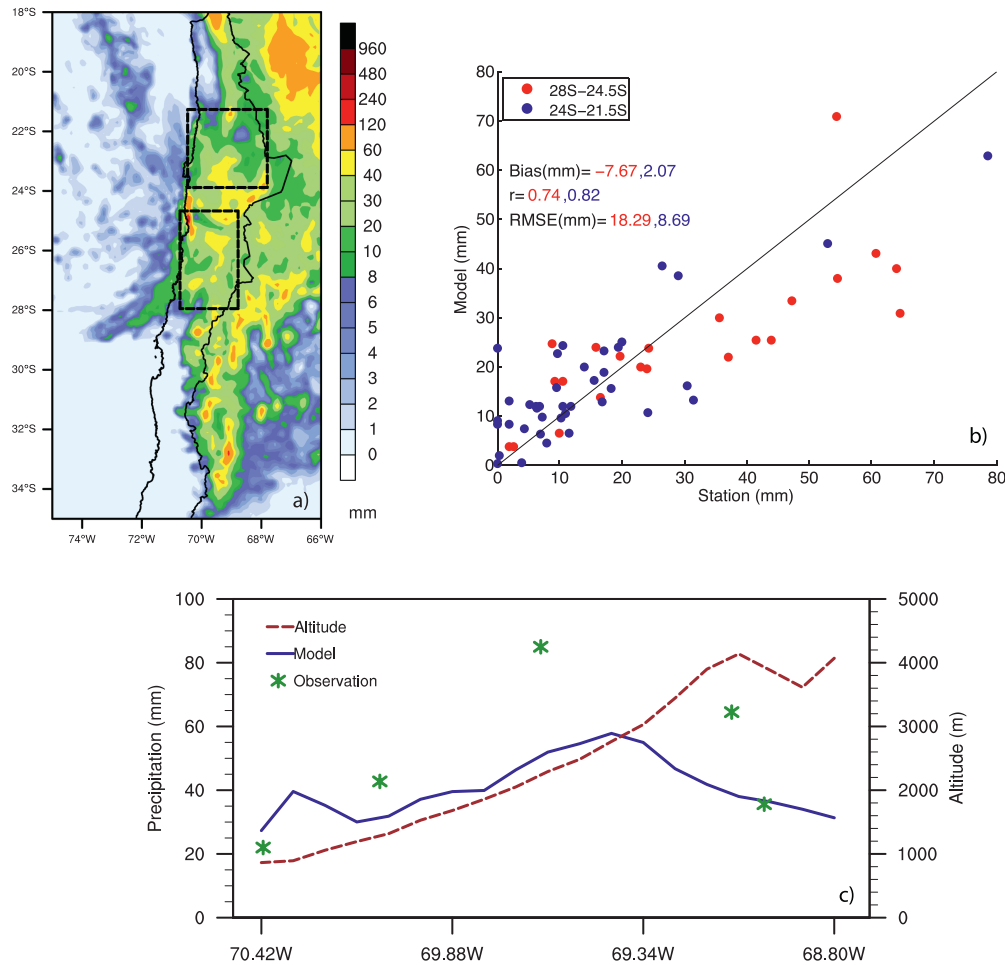


FIG. 12. (a) The 3-day (24–26 Mar 2015) accumulated precipitation (mm) in CTR and (b) scatterplot of 3-day accumulated precipitation from the observations and corresponding model grids (mm) over two boxes (red circles are for 28°–24.5°S and blue circles are for 24°–21.5°S). (c) The 3-day accumulated observed (local stations) and simulated zonal precipitation (mm) along 26°S.

the domain (eastern tropical Pacific coasts: 10°–15°S, 90°–78°W; and off northern Chile: 18°–24°S, 70.5°–72°W) show only slight differences (Fig. 13). This is an indication that altering the SST in the eastern Pacific has little impact on the regional-scale “dry” circulation (including the COL development off northern Chile), which downplays the role of the SST in altering the dynamics of COL through intensification of surface baroclinicity.

Altering the SST, however, does have an impact on thermodynamic aspects of the COL. To take a closer look at the differences between CTR and SENS, simulated vertical profiles of specific moisture and air temperature on 25 March are provided in Fig. 13. Over the eastern tropical Pacific (Fig. 13a), surface cooling extends in the vertical to about 750 hPa in SENS relative to CTR (1°–1.5°C) and consequently, SENS has higher static stability than CTR over this particular box.

Likewise, the tropical column in SENS shows a reduction of about  $1.5 \text{ g kg}^{-1}$  between the surface and 500 hPa with respect to CTR. Off the coast of northern Chile (Fig. 13b), the air temperature differences between the simulations are very small (consistent with the minor local SST changes) but the lower troposphere in SENS is still  $0.5\text{--}1 \text{ g kg}^{-1}$  (about 10% reduction) drier than in CTR. This strongly indicates that changes in the transport from the north, rather than changes in local evaporation, explain the moistening of the lower troposphere in northern Chile.

There is a substantial reduction in PW in SENS relative to CTR, not only over the eastern tropical Pacific but also in a band coincident with the tongue of moist air along the subtropical coast (contour in Fig. 11a). Again, we interpret this PW reduction at subtropical latitudes as a result of the reduction of horizontal transport of water vapor in the leading edge of the COL. The PW

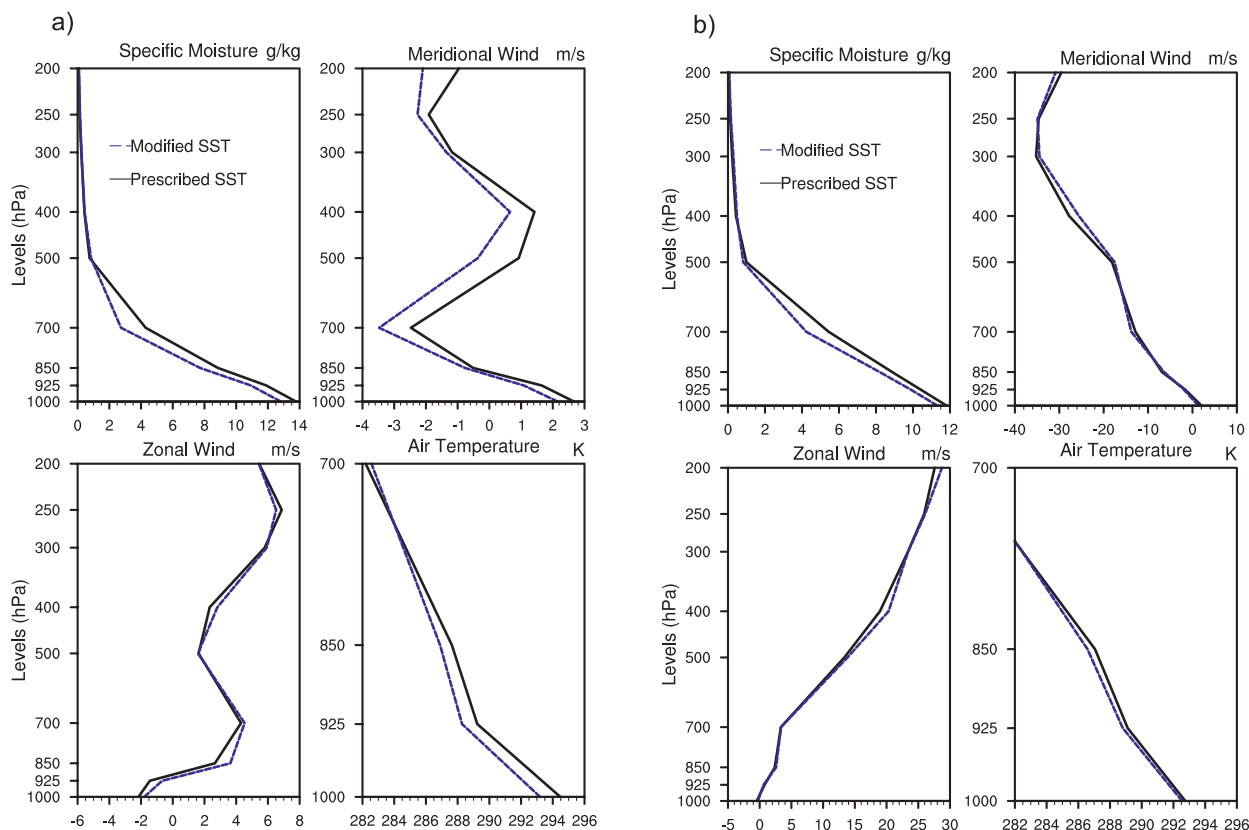


FIG. 13. (a) Vertical profiles of  $q$  ( $\text{g kg}^{-1}$ ),  $v$  ( $\text{m s}^{-1}$ ), zonal wind ( $\text{m s}^{-1}$ ), and air temperature (K) for CTR (black solid line) and SENS (blue dashed line) on 25 Mar 2015, averaged over ( $10^{\circ}$ – $15^{\circ}$ S,  $90^{\circ}$ – $78^{\circ}$ W). (b) As in (a), but for values averaged over ( $18^{\circ}$ – $24^{\circ}$ S,  $70.5^{\circ}$ – $72^{\circ}$ W) (see Fig. 9 for the boxes).

reduction off the coast of northern Chile in SENS ranges between 4 and 12 mm (Fig. 11b). This region is just to the east of the COL center where synoptically driven ascent occurs.

Given the reduction in PW one should expect a commensurate decrease in the storm-accumulated precipitation. Figure 14 shows the 3-day (24–26 March) accumulated precipitation differences between the SENS and CTR in absolute (Fig. 14a) and percentage values (Fig. 14b). Indeed, SENS shows a significant decrease in precipitation over most of northern Chile and the adjacent ocean relative to CTR. Between  $24^{\circ}$  and  $28^{\circ}$ S SENS suppressed total accumulations by 60%–80%. North of Antofagasta ( $23.5^{\circ}$ S) SENS suppresses precipitation almost entirely.

#### 4. Summary and conclusions

Between 24 and 26 March 2015, an extreme precipitation event took place in northern Chile, including the hyperarid Atacama Desert, which receives, on average, less than  $1 \text{ mm yr}^{-1}$ . The 1-day accumulated precipitation exceeded 40 mm (with hourly precipitation

rates of more than  $10 \text{ mm h}^{-1}$ ) in several locations, triggering flooding and landslides that resulted in casualties and significant damage. Only a handful precipitation events of this magnitude—often with catastrophic outcomes—have occurred in northern Chile during the last century, most (but not all) of them during El Niño years. Surface observations, complemented with snapshots of the event taken from radar instruments on board satellites, reveal two main periods of precipitation, one in the morning of 24 March and a second one, more extended in space, on 25 March. In both periods, we observed convective cells embedded in a broader area of stratiform precipitation over the coastal area and the inland desert. Accumulated precipitation maximized in those areas and then decreased gradually toward the higher terrain of the Andes Cordillera.

The synoptic-scale circulation was investigated using the European Centre for Medium-Range Weather Forecasts (ECMWF) interim reanalysis, surface, and radiosonde data. An intense, quasi-stationary upper-level ridge/surface anticyclone over the South Pacific near the tip of South America set the stage for the

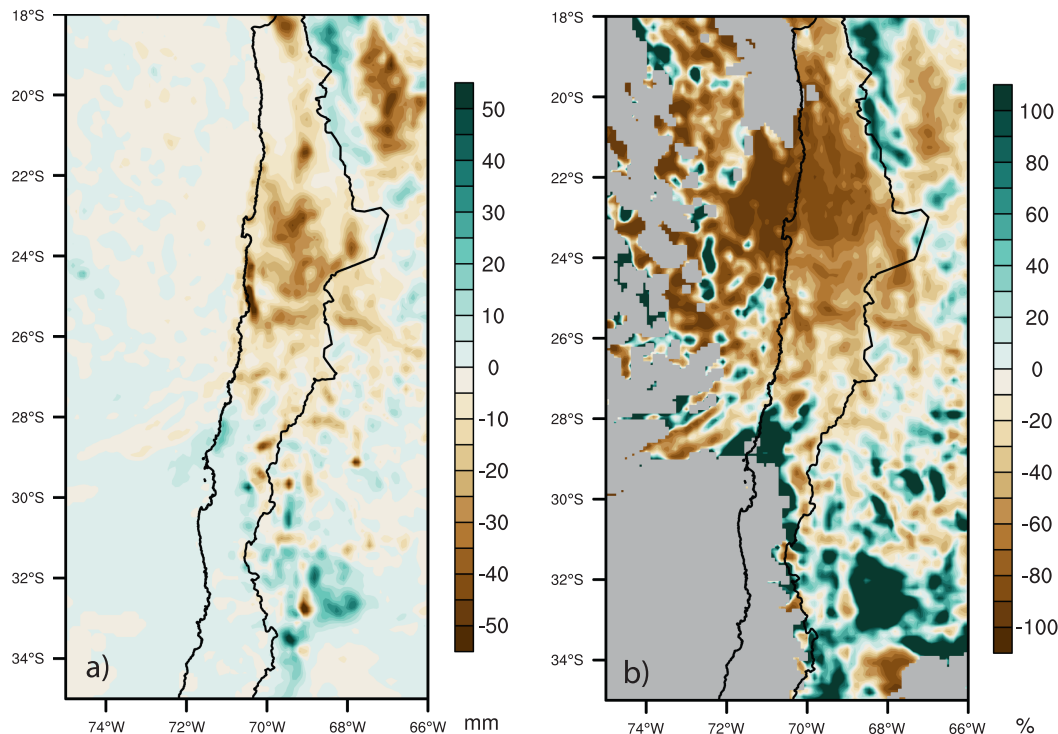


FIG. 14. The 3-day (24–26 Mar 2015) accumulated (a) absolute (mm) and (b) relative (%) precipitation differences between SENS and CTR. Percentage values are obtained by multiplying the ratio of  $(\text{SENS} - \text{CTR})/\text{CTR}$  by 100. Grid points where the 3-day accumulated precipitation is smaller than 0.5 mm in CTR are masked (gray shaded).

formation of a cutoff low (COL) at subtropical latitudes. The center of the COL reached its northernmost latitude of  $\sim 27^{\circ}\text{S}$  near the coast of northern Chile having a maximum strength on 25 March. This pattern of ridge formation and amplifying of upper-level troughs has been reported in previous COL episodes over different regions in the world (e.g., Bell and Bosart 1993; Mishra et al. 2001; Blamey and Reason 2009) and particularly over the subtropical southeastern Pacific, where a COL passage is not infrequent (e.g., Garreaud and Fuenzalida 2007; Barahona et al. 2015; Fuenzalida et al. 2005). The circulation around the COL was instrumental for the precipitation event in three ways. First, it provided a broad area of midlevel ascending motion to the east of its center. Second, midlevel northwesterly flow ahead of the COL impinged the Andes Cordillera, producing another sector of strong ascending motion over the sloping terrain. Finally, the same northwesterly flow at mid- and lower levels transported moist air along the western coast of South America from the equatorial eastern Pacific down to northern Chile where it eventually fed into the rainfall over Atacama.

A simple frequency analysis of the COL-related circulation features (e.g., minimum geopotential height at its center) revealed strong but not extreme dynamical

conditions during this event. In contrast, the period 24–26 March 2015 has the most extreme moist conditions [as per vertically integrated precipitable water (PW)] during austral fall in coastal northern Chile during the last 35 years. We hypothesized that such anomalous moistening of the lower free troposphere off northern Chile was key in producing the high rainfall rates over Atacama and, in turn, was associated with a substantial warming of the sea surface over the eastern tropical Pacific during the second week of March 2015, heralding the onset of a strong El Niño year.

We were able to test our hypothesis conducting a numerical experiment using the RegCM4 regional atmospheric model. A control RegCM4 simulation (forced with observed SST) realistically represented the main dynamical features of the COL at the time of the storm. Despite this reasonable agreement the model has some difficulty reproducing the exact location of the COL center and underestimates PW amounts over the region. The simulated precipitation agrees quite well with the observed pattern over Atacama and the simulated values match the observations over the arid zone well. However, underestimation of precipitation occurs to the south of  $28^{\circ}\text{S}$  probably due to the lower PW transported southward parallel to the coast and

inconsistencies in the COL center. SENS, which removes the warm SST anomaly in the eastern tropical Pacific, reproduces COL dynamics very similar to that in CTR. It is clear from SENS that a cooler SST forcing in the eastern tropical Pacific results in significant reduction in PW immediately over the SST anomaly as well as over the tongue of high PW ahead of the COL center. This dramatic reduction in PW appears as the main cause in the reduction of precipitation by 60%–80% over northern Chile and 100% in parts of the Atacama Desert, given the similar dry dynamics and local stability in both CTR and SENS over Atacama.

Thus, a key finding of our modeling experiment is that the warm coastal SST anomaly, favored by the onset of El Niño, was instrumental to the extreme precipitation event in Atacama by providing an anomalous source of water vapor in a synoptic environment that enhances upward motion. We have examined this event from a synoptic-scale perspective and, therefore, we have refrained here from dwelling on the origin of the eastern Pacific SST anomaly or the possible origin of the upper-level cyclonic anomaly. Indeed, both Madden–Julian oscillation (MJO) and ENSO had the right phase and intensity to induce an atmospheric teleconnection favorable for the occurrence of a COL in northern Chile (Juliá et al. 2012; Rutllant and Fuenzalida 1991; Vargas et al. 2000) and the warming in the eastern tropical Pacific. Given the rarity and extremeness of the event and also the large region affected, more research is warranted to further clarify the mechanisms that led to this extreme event both at the large hemispheric scale and also at the mesoconvective scale.

*Acknowledgments.* This study was supported by Fondo de Financiamiento de Centros de Investigación en Áreas Prioritarias (FONDAP)/Comisión Nacional de Investigación Científica y Tecnológica (CONICYT) Chile (Grant 15110009-CR2). Deniz Bozkurt also acknowledges Fondo Nacional de Desarrollo Científico y Tecnológico (FONDECYT)-Chile (Grant 3150036) for a postdoctoral fellowship. Powered@NLHPC: This research was partially supported by the supercomputing infrastructure of the National Laboratory for High Performance Computing (NLHPC) (ECM-02). Rainfall data from Paranal Observatory were kindly provided by Florian Kerber from the European Southern Observatory (ESO). Rainfall data from Corporación Nacional del Cobre (CODELCO)-Salvador mining operations are also acknowledged. GPM Dual-Frequency Precipitation Radar data were downloaded from the NASA Precipitation Processing System (doi:10.5067/GPM/DPR/DPR/2A). The authors also acknowledge two anonymous reviewers for their constructive comments that helped to improve the manuscript.

## REFERENCES

- Abarca, S. F., K. L. Corbosiero, and T. J. Galarneau Jr., 2010: An evaluation of the Worldwide Lightning Location Network (WWLLN) using the National Lightning Detection Network (NLDN) as ground truth. *J. Geophys. Res.*, **115**, D18206, doi:10.1029/2009JD013411.
- Aceituno, P., M. R. Prieto, M. E. Solari, A. Martínez, G. Poveda, and M. Falvey, 2009: The 1877–1878 El Niño episode: Associated impacts in South America. *Climatic Change*, **92**, 389–416, doi:10.1007/s10584-008-9470-5.
- Anthes, R. A., 1977: A cumulus parameterization scheme utilizing a one-dimensional cloud model. *Mon. Wea. Rev.*, **105**, 270–286, doi:10.1175/1520-0493(1977)105<0270:ACPSUA>2.0.CO;2.
- Bao, X., and F. Zhang, 2013: Evaluation of NCEP–CFRSR, NCEP–NCAR, ERA-Interim, and ERA-40 reanalysis datasets against independent sounding observations over the Tibetan Plateau. *J. Climate*, **26**, 206–214, doi:10.1175/JCLI-D-12-00056.1.
- Barahona, C., R. Garreaud, and R. Rondanelli, 2015: Precipitation associated with cut-off low (COL) systems in the Southern Hemisphere. *11th Int. Conf. on Southern Hemisphere Meteorology and Oceanography*, Santiago, Chile, Universidad de Chile, Abstract 336.
- Barrett, B. S., D. A. Campos, J. Vincencio Veloso, and R. Rondanelli, 2016: Extreme temperature and precipitation events in March 2015 in central and northern Chile. *J. Geophys. Res. Atmos.*, **121**, 4563–4580, doi:10.1002/2016JD024835.
- Bell, G., and L. F. Bosart, 1993: A case study diagnosis of the formation of an upper-level cutoff cyclonic circulation over the eastern United States. *Mon. Wea. Rev.*, **121**, 1635–1655, doi:10.1175/1520-0493(1993)121<1635:ACSDOT>2.0.CO;2.
- Blamey, R. C., and C. J. C. Reason, 2009: Numerical simulation of a mesoscale convective system over the east coast of South Africa. *Tellus*, **61A**, 17–34, doi:10.1111/j.1600-0870.2008.00366.x.
- Davis, N., J. Bowden, F. Semazzi, L. Xie, and B. Onol, 2009: Customization of RegCM3 regional climate model for eastern Africa and a tropical Indian Ocean domain. *J. Climate*, **22**, 3595–3616, doi:10.1175/2009JCLI2388.1.
- Dee, D. P., and Coauthors, 2011: The ERA-Interim reanalysis: Configuration and performance of the data assimilation system. *Quart. J. Roy. Meteor. Soc.*, **137**, 553–597, doi:10.1002/qj.828.
- Departamento de Geofísica, Universidad de Chile, 2015: Caracterización meteorológica de la tormenta del 24 al 26 de Marzo de 2015 en Atacama y Antofagasta (Meteorological characterization of the 24–26 March 2015 storm in Atacama and Antofagasta). Departamento de Geofísica, Universidad de Chile (DGF), 38 pp.
- Dickinson, R. E., A. Henderson-Sellers, and P. J. Kennedy, 1993: Biosphere–Atmosphere Transfer Scheme (BATS) version 1e as coupled to the NCAR Community Climate Model. NCAR Tech. Note NCAR/TN-387+STR, NCAR, Boulder, CO, 72 pp. [Available online at <http://nldr.library.ucar.edu/repository/assets/technotes/TECH-NOTE-000-000-000-198.pdf>.]
- Emanuel, K. A., 1991: A scheme for representing cumulus convection in large-scale models. *J. Atmos. Sci.*, **48**, 2313–2335, doi:10.1175/1520-0469(1991)048<2313:ASFRCC>2.0.CO;2.
- ENFEN, 2015: Informe Técnico ENFEN. Tech. Rep. 03-2015, Comité Multisectorial Encargado Del Estudio Nacional Del Fenómeno El Niño, Perú, 29 pp.



- Fuenzalida, H. A., R. Sánchez, and R. D. Garreaud, 2005: A climatology of cutoff lows in the Southern Hemisphere. *J. Geophys. Res.*, **110**, D18101, doi:10.1029/2005JD005934.
- Garreaud, R. D., and J. Rutllant, 1996: Análisis meteorológico de los aluviones de Antofagasta y Santiago de Chile en el periodo 1991–1993 (Meteorological analysis of the Antofagasta and Santiago, Chile, debris flows in the 1991–1993 period). *Atmósfera*, **9**, 251–271.
- , and H. A. Fuenzalida, 2007: The influence of the Andes on cutoff lows: A modeling study. *Mon. Wea. Rev.*, **135**, 1596–1613, doi:10.1175/MWR3350.1.
- , A. Molina, and M. Farias, 2010: Andean uplift, ocean cooling and Atacama hyperaridity: A climate modeling perspective. *Earth Planet. Sci. Lett.*, **292**, 39–50, doi:10.1016/j.epsl.2010.01.017.
- Giorgi, F., M. R. Marinucci, and G. T. Bates, 1993a: Development of a second generation regional climate model (RegCM2). Part I: Boundary layer and radiative transfer processes. *Mon. Wea. Rev.*, **121**, 2794–2813, doi:10.1175/1520-0493(1993)121<2794:DOASGR>2.0.CO;2.
- , —, —, and G. DeCanio, 1993b: Development of a second generation regional climate model (RegCM2). Part II: Convective processes and assimilation of lateral boundary conditions. *Mon. Wea. Rev.*, **121**, 2814–2832, doi:10.1175/1520-0493(1993)121<2814:DOASGR>2.0.CO;2.
- , and Coauthors, 2012: RegCM4: Model description and preliminary tests over multiple CORDEX domains. *Climate Res.*, **52**, 7–29, doi:10.3354/cr01018.
- Grell, G. A., 1993: Prognostic evaluation of assumptions used by cumulus parameterizations. *Mon. Wea. Rev.*, **121**, 764–787, doi:10.1175/1520-0493(1993)121<0764:PEOAUB>2.0.CO;2.
- , J. Dudhia, and D. R. Stauffer, 1994: A description of the Fifth-generation Penn State/NCAR Mesoscale Model (MM5). NCAR Tech. Note NCAR/TN-398+STR, NCAR, Boulder, CO, 121 pp.
- Holtstag, A. A. M., E. I. F. de Bruijn, and H. L. Pan, 1990: A high resolution air mass transformation model for short-range weather forecasting. *Mon. Wea. Rev.*, **118**, 1561–1575, doi:10.1175/1520-0493(1990)118<1561:AHRAMT>2.0.CO;2.
- Hoskins, B. J., M. E. McIntyre, and A. W. Robertson, 1985: On the use and significance of isentropic potential vorticity maps. *Quart. J. Roy. Meteor. Soc.*, **111**, 877–946, doi:10.1002/qj.49711147002.
- Hou, A. Y., and Coauthors, 2014: The Global Precipitation Measurement mission. *Bull. Amer. Meteor. Soc.*, **95**, 701–722, doi:10.1175/BAMS-D-13-00164.1.
- Houston, J., 2006: Variability of precipitation in the Atacama Desert: Its causes and hydrological impact. *Int. J. Climatol.*, **26**, 2181–2198, doi:10.1002/joc.1359.
- Iguchi, T., T. Kozu, R. Meneghini, J. Awaka, and K. Okamoto, 2000: Rain-profiling algorithm for the TRMM Precipitation Radar. *J. Appl. Meteor.*, **39**, 2038–2052, doi:10.1175/1520-0450(2001)040<2038:RPAFTT>2.0.CO;2.
- Juliá, C., D. A. Rahn, and J. A. Rutllant, 2012: Assessing the influence of the MJO on strong precipitation events in subtropical, semi-arid north-central Chile (30°S). *J. Climate*, **25**, 7003–7013, doi:10.1175/JCLI-D-11-00679.1.
- Kiehl, J. T., J. J. Hack, G. B. Bonan, B. A. Boville, B. P. Breigleb, D. Williamson, and P. Rasch, 1996: Description of the NCAR Community Climate Model (CCM3). NCAR Tech. Note NCAR/TN-420+STR, NCAR, Boulder, CO, doi:10.5065/D6FF3Q99.
- Kumar, A., R. A. Houze Jr., K. L. Rasmussen, and C. Peters-Lidard, 2014: Simulation of a flash flooding storm at the steep edge of the Himalayas. *J. Hydrometeorol.*, **15**, 212–228, doi:10.1175/JHM-D-12-0155.1.
- Lettau, H. H., and K. Lettau, 1978: *Explaining the World's Driest Climate*. University of Wisconsin Press, 264 pp.
- Marshall, A. G., H. H. Hendon, and G. Wang, 2016: On the role of anomalous ocean surface temperatures for promoting the record Madden–Julian oscillation in March 2015. *Geophys. Res. Lett.*, **43**, 472–481, doi:10.1002/2015GL066984.
- Middleton, N., 2003: *Going to Extremes*. Pan Books, 129 pp.
- Mishra, S. K., V. B. Rao, and M. A. Gan, 2001: Structure and evolution of the large-scale flow and an embedded upper-tropospheric cyclonic vortex over northeast Brazil. *Mon. Wea. Rev.*, **129**, 1673–1688, doi:10.1175/1520-0493(2001)129<1673:SAEOTL>2.0.CO;2.
- Muller, A., C. Reason, and N. Fauchereau, 2008: Extreme rainfall in the Namib Desert during late summer 2006 and influences of regional ocean variability. *Int. J. Climatol.*, **28**, 1061–1070, doi:10.1002/joc.1603.
- Muñoz, R. C., R. A. Zamora, and J. A. Rutllant, 2011: The coastal boundary layer at the eastern margin of the southeast Pacific (23.4°S, 70.4°W): Cloudiness-conditioned climatology. *J. Climate*, **24**, 1013–1033, doi:10.1175/2010JCLI3714.1.
- Olson, D. M., and Coauthors, 2001: Terrestrial ecoregions of the world: A new map of life on Earth. *BioScience*, **51**, 933–938, doi:10.1641/0006-3568(2001)051[0933:TEOTWA]2.0.CO;2.
- ONEMI, 2015: Oficina Nacional de Emergencia del Ministerio del Interior. Accessed 6 July 2015. [Available online at <http://www.onemi.cl/alerta/monitoreo-por-evento-hidrometeorologico/>].
- Pal, J. S., E. E. Small, and E. A. B. Eltahir, 2000: Simulation of regional-scale water and energy budgets: Representation of surged cloud and precipitation processes within RegCM. *J. Geophys. Res.*, **105**, 29 579–29 594, doi:10.1029/2000JD900415.
- , and Coauthors, 2007: Regional climate modeling for the developing world: The ICTP RegCM3 and RegCNET. *Bull. Amer. Meteor. Soc.*, **88**, 1395–1409, doi:10.1175/BAMS-88-9-1395.
- Palmén, E., 1949: On the origin and structure of high-level cyclones south of the maximum westerlies. *Tellus*, **1A**, 22–25, doi:10.1111/j.2153-3490.1949.tb01925.x.
- Rasmussen, K. L., and R. A. Houze Jr., 2012: A flash flooding storm at the step edge of high terrain: Disaster in the Himalayas. *Bull. Amer. Meteor. Soc.*, **93**, 1713–1724, doi:10.1175/BAMS-D-11-00236.1.
- Rondanelli, R., A. Molina, and M. Falvey, 2015: The Atacama surface solar maximum. *Bull. Amer. Meteor. Soc.*, **96**, 405–418, doi:10.1175/BAMS-D-13-00175.1.
- Rutllant, J., and H. Fuenzalida, 1991: Synoptic aspects of the central Chile rainfall variability associated with the Southern Oscillation. *Int. J. Climatol.*, **11**, 63–76, doi:10.1002/joc.3370110105.
- , —, and P. Aceituno, 2003: Climate dynamics along the arid northern coast of Chile: The 1997–1998 Diclima Experiment. *J. Geophys. Res.*, **108**, 4538–4542, doi:10.1029/2002JD003357.
- Satoh, M., T. Nasuno, H. Miura, H. Tomita, S. Iga, and Y. Takayabu, 2008: Precipitation statistics comparison between global cloud resolving simulation with NICAM and TRMM PR data. *High Resolution Numerical Modelling of the Atmosphere and Ocean*. K. Hamilton and W. Ohfuchi, Eds., Springer, 99–112.
- Schulz, N., J. P. Boisier, and P. Aceituno, 2012: Climate change along the arid coast of northern Chile. *Int. J. Climatol.*, **32**, 1803–1814, doi:10.1002/joc.2395.
- Sepúlveda, S. A., S. Rebelled, and G. Vargas, 2006: Recent catastrophic debris flows in Chile: Geological hazard, climatic relationships and human response. *Quat. Int.*, **158**, 83–95, doi:10.1016/j.quaint.2006.05.031.

- Smiatek, G., H. Kunstmann, R. Knoche, and A. Marx, 2009: Precipitation and temperature statistics in high-resolution regional climate models: Evaluation for the European Alps. *J. Geophys. Res.*, **114**, D19107, doi:10.1029/2008JD011353.
- Sylla, M. B., F. Giorgi, P. M. Ruti, S. Calmanti, and A. Dell'Aquila, 2011: The impact of deep convection on the West African summer monsoon climate: A regional climate model sensitivity study. *Quart. J. Roy. Meteor. Soc.*, **137**, 1417–1430, doi:10.1002/qj.853.
- Takahashi, K., 2004: The atmospheric circulation associated with extreme rainfall events in Piura, Peru, during the 1997–1998 and 2002 El Niño events. *Ann. Geophys.*, **22**, 3917–3926, doi:10.5194/angeo-22-3917-2004.
- University of Wyoming, 2015: Upper air observations. Department of Atmospheric Sciences, University of Wyoming, accessed April 2015. [Available online at <http://weather.uwyo.edu/upperair/sounding.html>.]
- Vargas, G., L. Ortlieb, and J. Rutllant, 2000: Aluviones históricos en Antofagasta y su relación con eventos El Niño/Oscilación del Sur (Historical floods in Antofagasta and its relation with ENSO events). *Rev. Geol. Chile*, **27** (2), 157–176.
- Vicuña-Mackenna, B., 1877: *Ensayo Histórico sobre el Clima de Chile (Historical Essay on the Climate of Chile)*. Imprenta El Mercurio, Valparaiso, 490 pp.
- Vuille, M., and C. Ammann, 1997: Regional snowfall patterns in the high arid Andes. *Climatic Change*, **36**, 413–423, doi:10.1023/A:1005330802974.
- Wang, Y., O. L. Sen, and B. Wang, 2003: A highly resolved regional climate model (IPRC-RegCM) and its simulation of the 1998 severe precipitation event over China. Part I: Model description and verification of simulation. *J. Climate*, **16**, 1721–1738, doi:10.1175/1520-0442(2003)016<1721:AHRRCM>2.0.CO;2.
- Wilcox, A. C., and Coauthors, 2016: An integrated analysis of the March 2015 Atacama floods. *Geophys. Res. Lett.*, **43**, 8035–8043, doi:10.1002/2016GL069751.
- Zeng, X., M. Zhao, and R. E. Dickinson, 1998: Intercomparison of bulk aerodynamic algorithms for the computation of sea surface fluxes using TOGA COARE and TAO data. *J. Climate*, **11**, 2628–2644, doi:10.1175/1520-0442(1998)011<2628:IOBAAF>2.0.CO;2.
- Zhao, S., and J. Sun, 2007: Study on cut-off low-pressure systems with floods over northeast Asia. *Meteor. Atmos. Phys.*, **96**, 159–180, doi:10.1007/s00703-006-0226-3.